Received: 29 May 2024 | Revised: 15 January 2025 | Accepted: 15 January 2025

DOI: 10.1002/mp.17661

RESEARCH ARTICLE

MEDICAL PHYSICS

Technique selection and technical developments for 2D dual-energy subtraction angiography on an interventional C-arm

Ethan P. Nikolau[1] | **Joseph F. Whitehead**[1] | **Martin G. Wagner**[2] | **James R. Scheuermann**[3] | **Paul F. Laeseke**[2] | **Michael A. Speidel**[1,4]

[1]Department of Medical Physics, University of Wisconsin - Madison, Madison, Wisconsin, USA

[2]Department of Radiology, University of Wisconsin - Madison, Madison, Wisconsin, USA

[3]Siemens Healthineers, Malvern, Pennsylvania, USA

[4]Department of Medicine, University of Wisconsin - Madison, Madison, Wisconsin, USA

Correspondence
Michael A. Speidel, Department of Medical Physics, University of Wisconsin – Madison, 1111 Highland Ave, Rm 1005, Madison, WI 53705, USA.
Email: speidel@wisc.edu

Funding information
National Institutes of Health, Grant/Award Number: R21 EB023008; National Cancer Institute of the National Institutes of Health, Grant/Award Number: T32CA009206; Siemens Healthineers

Abstract

Background: Dual-energy (DE) x-ray image acquisition has the potential to provide material-specific angiographic images in the interventional suite. This approach can be implemented with novel detector technologies, such as dual-layer and photon-counting detectors. Alternatively, DE imaging can be implemented on existing systems using fast kV-switching. Currently, there are no commercially available DE options for interventional platforms.

Purpose: This study reports on the development of a prototype fast kV-switching DE subtraction angiography system. In contrast to alternative approaches to DE imaging in the interventional suite, this prototype uses a clinically available interventional C-arm equipped with special x-ray tube control software. An automatic exposure control algorithm and technical features needed for such a system in the interventional setting are developed and validated in phantom studies.

Methods: Fast kV-switching was implemented on an interventional C-arm platform using software that enables frame-by-frame specification of x-ray tube techniques (e.g., tube voltage/kV, pulse width/ms, tube current/mA). A real-time image display was developed on a portable workstation to display DE subtraction images in real-time (nominal 15 frame/s). An empirical CNR-driven automatic exposure control (AEC) algorithm was created to guide DE tube technique selection (kV pair, ms pair, mA). The AEC model contained a look-up table which related DE tube technique parameters and air kerma to iodine CNR, which was measured in acrylic phantom models containing an iodine-equivalent reference object. For a given iodine CNR request, the AEC algorithm estimated patient thickness and then selected the DE tube technique expected to deliver the requested CNR at the minimum air kerma. The AEC algorithm was developed for DE imaging performed without and with the application of anti-correlated noise reduction (ACNR). Validation of the AEC model was performed by comparing the AEC-predicted iodine CNR values with directly measured values in a separate phantom study. Both dose efficiency (CNR^2/kerma) and maximum achievable iodine CNR (within tube technique constraints) were quantified. Finally, improvements in DE iodine CNR were quantified using a novel variant to the ACNR approach, which used machine-learning image denoising (ACNR-ML).

Results: The prototype system provided a continuous display of DE subtraction images. For standard DE imaging, the AEC-predicted iodine CNR values agreed with directly measured values to within 3.5% ± 1.6% (mean ± standard deviation). When ACNR was applied, predicted iodine CNR agreed with measurement to within 2.1% ± 3.3%. AEC-generated DE techniques were typically (low/high energy): 63/125 kV, 10/3.2 ms, with varying mA values. When ACNR was applied, dose efficiency was increased by a factor of 9.37 ± 2.08 and maximum CNR was increased by a factor of 3.29 ± 0.21 relative to DE without denoising. Application of ACNR-ML yielded a greater increase in both the dose efficiency (16.11 ± 2.99) and maximum CNR (4.46 ± 0.31) compared to DE without denoising.

Conclusion: A prototype DE subtraction angiography system using fast kV-switching was implemented on a clinically available interventional C-arm platform without modification of system hardware. The technical features presented in this work include a real-time image display, noise-reduction strategies, and a CNR-driven AEC algorithm. This prototype system demonstrates the feasibility of 2D dual-energy imaging for image-guided interventions.

KEYWORDS
angiography, dual-energy, interventional imaging

1 | INTRODUCTION

Dual-energy (DE) imaging techniques employ two different x-ray spectra and exploit differences in material attenuation coefficient versus energy in order to differentiate, isolate, or quantify materials of interest within the body.[1] Established clinical applications include chest radiography,[2,3] bone mineral densitometry,[4] and recently, CT imaging.[5–7] Although there are currently no options available for clinical interventional x-ray angiography platforms, DE capability has been investigated,[8] and may offer several benefits to image-guided procedures. These include quantitation of injected radiopaque materials, and removal of tissue components which may move and cause artifacts during conventional digital subtraction angiography.[9,10]

The simplest method of acquiring x-ray image data at two distinct energies is sequential scanning, which involves consecutively imaging the patient with two different tube voltages. This can be implemented on any x-ray system, but is susceptible to misregistration artifacts, which manifest if there is internal or external patient motion between the scans. In applications where significant patient motion can occur (e.g., respiratory motion, cardiac motion), it is desirable to minimize the temporal separation between the low and high-energy data used to form each DE image. Recent research has focused on the use of novel detector technologies such as dual-layer flat-panel detectors[11–13] and photon-counting detectors[14–18] as a means to simultaneously acquire low- and high-energy projection images, among other benefits. However, this detector hardware is not yet available on clinical interventional platforms. Alternatively, DE imaging could be implemented on existing platforms using fast x-ray tube voltage switching, similar to the strategy employed in some dual-energy CT systems.[5,6] Recently, software-driven fast kV-switching at up to 30 Hz was reported on an interventional system.[8,19] This approach does not require hardware modification and enables real-time 2D dual-energy angiography or fluoroscopy imaging with minimal time separation between low- and high-energy images.

This paper presents a prototype fast kV-switching DE imaging system for 2D angiographic procedures within the interventional suite. In previous work, the accuracy of the software-driven x-ray tube control was reported, and application to free-breathing pulmonary angiography was proposed.[19] The present study extends development of this prototype DE system, with a focus on the development of technical features expected in a clinical system. The key contributions of this work are: (i) development of a real-time DE imaging display and a method for displaying material-subtracted images, (ii) an investigation of two noise-reduction strategies, and (iii) development of a contrast-to-noise ratio (CNR) driven automatic exposure control (AEC) algorithm for determining the DE tube technique (kV, mA, and ms for high- and low-energy beams) with the minimum air kerma in a given imaging setting. Testing and validation are reported in phantom studies.

2 | MATERIALS AND METHODS

The following sections outline the method for developing features for an interventional x-ray platform with fast kV-switching capability. First, the interventional platform and fast kV-switching implementation are described. Next,

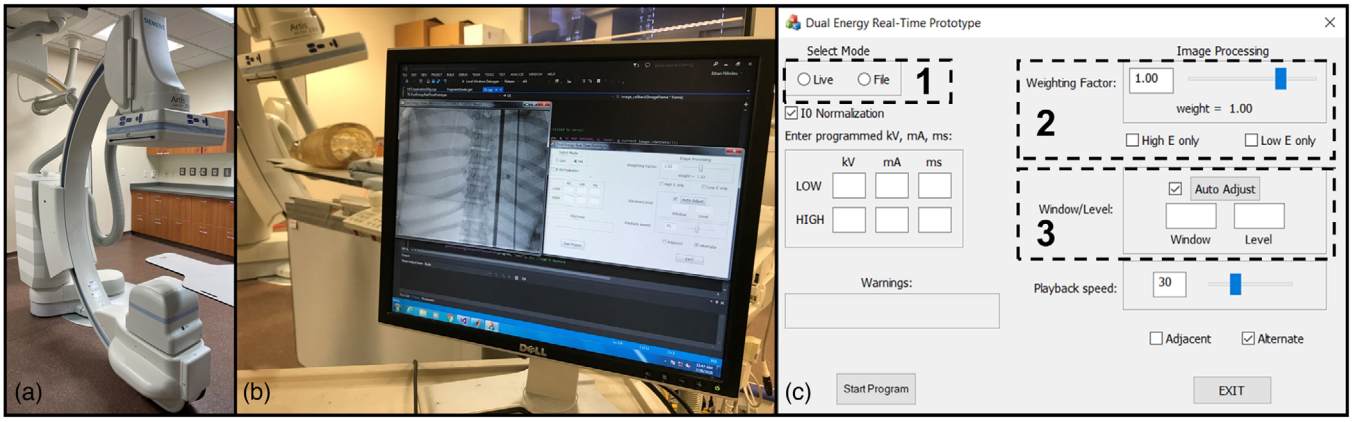

FIGURE 1 (a) Siemens Artis zee interventional C-arm platform. (b) Portable workstation situated near the C-arm system, containing the real-time display (showing a DE image of a phantom) and a user-interface. (c) User-interface which contains certain features related to the DE image processing, including (1) the ability to view live images or load from file, (2) adjust the material-canceling weighting factor, and (3) automatic image window/level adjustment.

image processing techniques are described, including the formation of material-subtracted DE images, the real-time display system, and two image noise reduction approaches: the anti-correlated noise reduction algorithm (ACNR)[10] and an ACNR variant which uses machine-learning.[20] Finally, the development and validation of an automatic exposure control (AEC) algorithm are described.

2.1 | Interventional platform and DE source control

The interventional x-ray angiography system (Artis zee, Siemens Healthineers, Forchheim, Germany) for this work was equipped with a 30 cm × 40 cm flat panel detector (0.154 mm native element pitch), and a Megalix Cat+ x-ray tube capable of operating at up to 125 kV, 80 kW (nominal) power using the 1.0 mm focal spot. In the prototype fast kV-switching DE mode, the magnification factor was set to utilize the entire field of view, and 2 × 2 pixel binning was used to achieve a 0.308 mm element pitch. The anti-scatter grid was a focused linear grid with 15:1 grid ratio and 80 lines/cm. This x-ray system (Figure 1a) is dedicated to research.

The fast kV-switching implementation was based on prototype x-ray tube control software previously developed by Mueller et al.[8] In short, the software implements a rotational acquisition mode that delivers an x-ray tube technique specified by the user. The tube voltage (kV), tube current (mA), and pulse width (ms) are specified on a frame-by-frame basis. A fast kV-switching mode normally uses two kV values, two ms values, and a single mA value for each pair of images. Validation of kV and ms modulation at up to 30 Hz was performed in prior work using a RadCal AccuGold meter with an AGMS-D+ sensor.[19] Using this approach, projection data can be acquired at up to 30 Hz for arbitrary fast kV-switching DE techniques (kV pair, mA, ms pair), as long as the technique adheres to tube loading and operational constraints. DE images can be formed at 15 frame/s using the unique pairs of low- and high-energy projections acquired at 30 Hz.

2.2 | Dual-energy image formation and real-time display

Real-time DE images were formed using the weighted log subtraction method. This method can be used to selectively subtract, or cancel the signal from materials in projection images.[9,21] Following previous investigations of DE digital subtraction angiography, this approach was used to subtract soft tissue signal and isolate iodine/bone signal.[9,10] Given a temporally adjacent pair of logged low- and high-energy projection images, L and H, the *iodine/bone-only* DE image was computed as,

$$I = L - w_t H, \tag{1}$$

where w_t is the weighting factor that cancels tissue signal in the image. Theoretically, the material-canceling weighting factor represents a ratio of mass attenuation coefficients at low versus high energy for the material to be canceled; materials having the same ratio (e.g., soft tissues, blood, air) are subtracted at the same time. In practice, automatic determination of this factor is challenging due to scattered radiation, which creates a bias in the expected value. Recently, an analytical approach for predicting DE weighting factors has been discussed.[22] Alternatively, weighting factors can be set empirically by minimizing the signal difference between two neighboring regions which contain varying thicknesses of the material of interest.[23]

A *tissue-only* DE image was formed from the same projection data with,

$$T = L - w_i H, \tag{2}$$

where w_i is the iodine/bone canceling factor. Although this tissue-only image is not needed for angiographic visualization of injected contrast agents, it was used for the denoising method described in Section 2.3.

Real-time DE image subtraction and display were implemented in C++ and OpenGL on a workstation equipped with a real-time image feed from the x-ray system. The workstation was a Dell 5810 XL tower equipped with 72 GB RAM and a GeForce 1080Ti GPU. Live, unprocessed image data were transmitted from the x-ray system to the workstation using a packet-based protocol over an ethernet connection to an Intel i217 network controller in the workstation. On the reciever side, the pcap library was used to retrieve packets of image data from the network and reassemble the images. Custom software on the workstation provided the live DE display as well as a user interface for adjusting the window/level, the material-canceling weighting factor, and other aspects of image recording. Figure 1b shows the real-time image display and user interface of the portable workstation.

Performance of the real-time processing and display was quantified by comparing the live frame rate against the nominal frame/s of the scan for a total of five 30 frame/s rotational acquisitions (248 frames total, or 124 displayed DE frames) in a series of stopwatch timing tests. As a point of comparison, this test was repeated for the built-in display of the x-ray system when operated in conventional single-energy mode. The precision of each timing measurement was assumed to be 200 ms.[24] Additionally, the total number of displayed DE image frames was recorded within the software using 20 acquisitions of varying durations (range: 3.2–10.1 s) for a total of 2350 DE image frames. The difference between the number of expected versus displayed image frames, or the amount of dropped frames, was quantified for each acquisition. Dropped frames were then reported as the mean and standard deviation of the individual percentages of these differences. Finally, the maximum DE image frame rate supported by the system was quantified by loading raw image frames into local memory and programmatically recording the amount of time required for the software to display a total of 1000 DE image frames without restriction on display rate. The maximum frame rate was reported as the mean and standard deviation across 10 repeat trials.

2.3 | Dual-energy image noise reduction

A noise-reduction algorithm specific to the DE subtraction approach was investigated for use on the prototype interventional DE system. The approach was based upon the ACNR algorithm,[10,25] which exploits 2D noise correlations in material-subtracted images to reduce image noise. A simple implementation of ACNR suitable for 2D angiography is,

$$I_{ACNR} = I - p\,(T - T_{LPF})\,, \tag{3}$$

where I_{ACNR} is the denoised iodine/bone-only image, I and T are the images formed by Equations (1) and (2), p is an adjustable ACNR factor, and T_{LPF} is the low-pass filtered tissue-only image. In practice, T_{LPF} is obtained by convolving T with an averaging kernel of $k \times k$ pixels. The ACNR factor p can be determined empirically by maximizing the CNR of an iodinated structure.[10]

The ACNR method of DE noise reduction[22,26–28] is well suited to the real-time nature of 2D angiographic imaging due to its simplicity. Furthermore, this approach carries the benefit that the iodine-filled vasculature is theoretically unaffected by the denoising operation since the filtering only occurs on a tissue-only image. However, the technique allows low-frequency noise components to remain in the final denoised DE image, which can impact SNR improvement and noise texture.[26] Additionally, the low-pass filtering operation risks blurring edge-like features of the tissue image (e.g., tissue/air boundaries), leading to inaccurate restoration of the tissue signal. To address these issues, a variant to the ACNR approach referred to as ACNR-ML was developed.[20] This alternative noise-reduction approach utilizes machine learning (ML) to denoise the tissue image rather than low-pass filtering. The formula for the iodine/bone-only image with ACNR-ML denoising is

$$I_{ACNR-ML} = I - p\,(T - T_{ML})\,. \tag{4}$$

In previous work, it was found that ACNR-ML can provide a further reduction in DE image noise compared to using ACNR alone, while also maintaining a noise texture more consistent with the original projection images.[20] Although the training of the ML model can require significant training time, the inference times for a trained model can be short and therefore suitable for real-time imaging applications. The ML model used in this work was based on a U-Net architecture,[29] and was trained on synthetic hepatic angiograms with and without simulated image noise. Details regarding the ML model training and the analysis of ACNR-ML noise texture can be found in previous work.[20,30]

2.4 | CNR-driven automatic exposure control (AEC)

For each pair of images in a fast kV-switching DE scheme, five x-ray tube parameters must be specified as follows: tube voltage (kV) and pulse width (ms) for

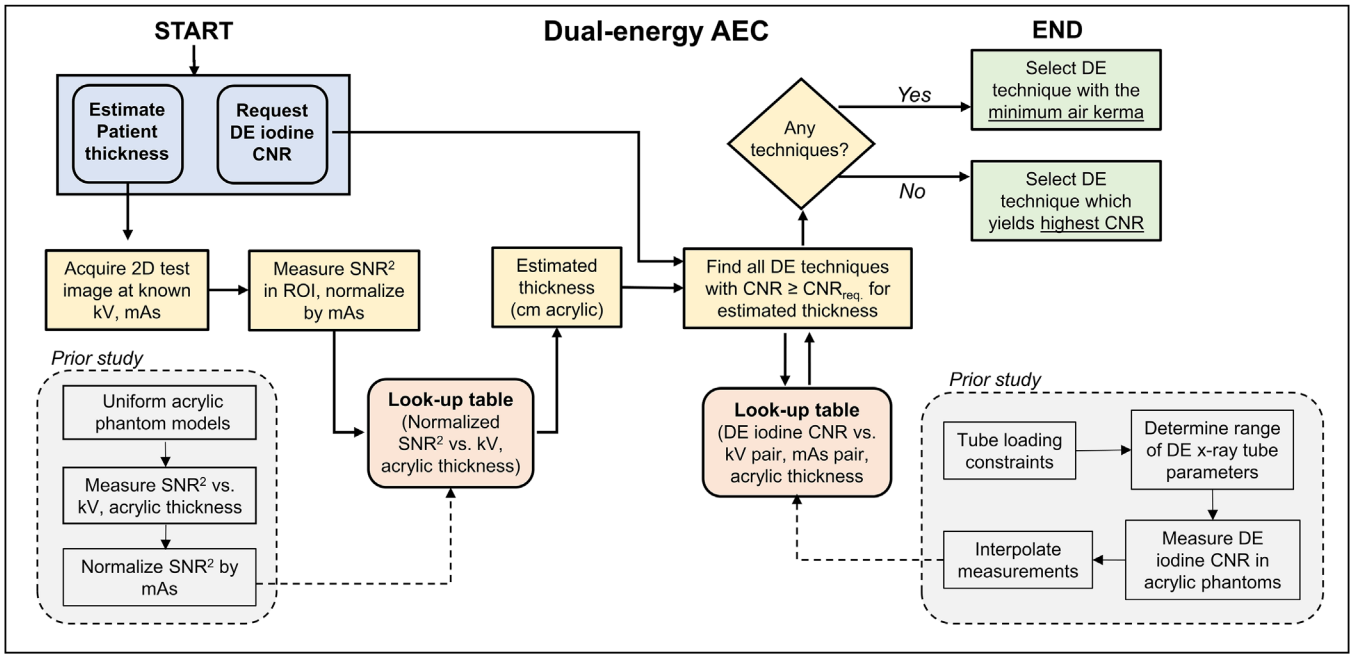

FIGURE 2 Overview of the AEC model used to generate fast kV-switching DE techniques. Both the iodine CNR request (determined prior to the study) and the estimated patient thickness (determined at the start of the study) are inputs to the AEC model. The AEC then finds all DE techniques which yield the CNR request for the given patient thickness using a look-up table. Finally, the AEC model selects the DE technique with the minimum air kerma (if there are valid techniques), or the DE technique which yielded the highest CNR value (if there are no valid techniques).

the high-energy image, kV and ms for the low-energy image, and tube current (mA) for both images. An AEC algorithm was developed to automate the selection of these DE tube parameters. The AEC relies on an empirical lookup table which relates DE tube techniques to an achieved CNR with an iodine-equivalent reference object and acrylic phantoms of varying thicknesses. In practice, the user specifies a desired iodine CNR and estimated patient thickness to the AEC, which then utilizes the look-up table (LUT) to determine the DE tube technique which delivers the requested CNR at the minimum possible air kerma. An overview of the AEC model used for fast kV-switching DE technique generation is shown in Figure 2. In this work, DE tube techniques were generated with and without the application of ACNR denoising. Separate techniques were not generated for the ACNR-ML algorithm; rather, ACNR-ML was used to explore further improvements in CNR relative to the ACNR algorithm, when using an ACNR tube technique.

2.4.1 | Estimating acrylic-equivalent patient thickness

The AEC algorithm used a pre-established LUT to estimate the acrylic-equivalent patient thickness in a given imaging geometry. Uniform acrylic phantoms of varying thicknesses (18.6–30.3 cm acrylic, in steps of 2.3 cm) were imaged at different tube voltage levels (55–125 kV in steps of 5 kV). The mAs values were chosen such that the image signal in the projection images remained constant. For each combination of kV and acrylic thickness, the image SNR was measured, and the squared SNR divided by mAs was stored in a table. These normalized squared SNR measurements were then interpolated with 2D spline curves across both acrylic thickness (0.1 cm increments) and tube voltage (1 kV increments).

To estimate the acrylic-equivalent patient thickness at the beginning of a DE imaging sequence, a single tube technique (kV and mAs) was used to acquire a reference x-ray projection image. The tube technique for the reference image was guided by a conventional single-energy AEC. A SNR measurement was made from the reference image using an ROI placed over the target anatomical region. The SNR value was then squared and normalized by the mAs value used to acquire the reference image. The acrylic-equivalent thickness corresponding to the ROI was then inferred by comparing the measured, normalized SNR value against the corresponding values in the LUTs for the same kV.

2.4.2 | Tube technique constraints

The investigated tube parameter space was chosen to adhere to vendor-provided x-ray tube rating charts, which specify recommended tube technique constraints, or operating limits that should not be exceeded. These

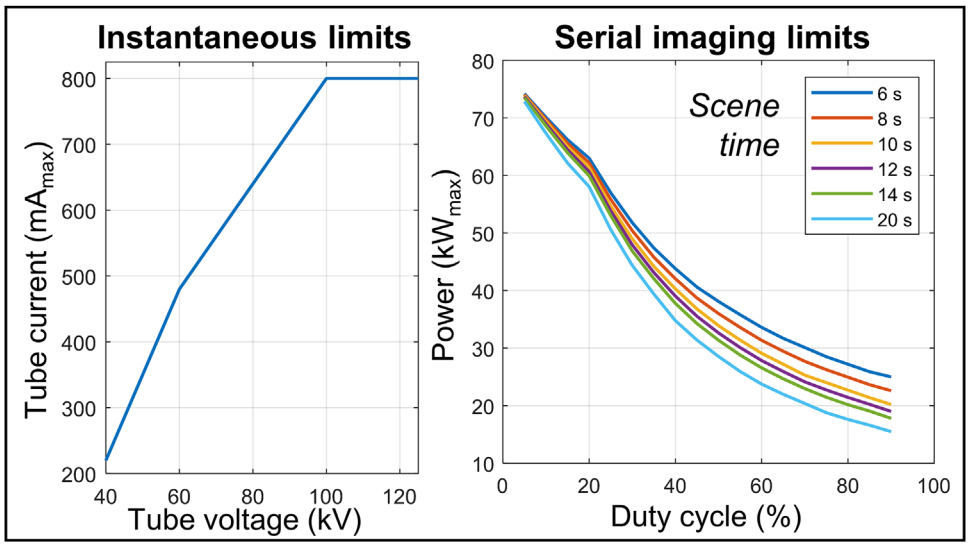

FIGURE 3 X-ray tube rating charts for single-energy acquisitions, using the 1.0 mm focal spot size. The instantaneous limits show the maximum tube current as a function of tube voltage. The serial imaging limits define the maximum power as a function of duty cycle, scene time, and focus spot size for single-energy imaging.

tube rating charts are shown in Figure 3 for single-energy imaging (not kV-switched) and a large focal spot size (1.0 mm). To determine the safety of an arbitrary fast kV-switching DE technique, defined as a kV pair, ms pair, and mA value, the instantaneous tube current limits were first evaluated. This process involves comparing the candidate mA value with the maximum mA allowed for each kV value in the DE kV pair, and rejecting the technique if the mA exceeds either maximum value. Next, the serial imaging limits were evaluated. First, the duty cycle was calculated, which was defined as the sum of the DE ms pair divided by two frame periods (2 × 33.3 ms). The maximum power was then inferred from charts containing the relationship between tube power, duty cycle, scene time (10.0 s), and focal spot size (1.0 mm). Next, this power limit was compared with the calculated power (kV × mA/1000) for both kV values in the kV pair. The technique was rejected if either calculated power value exceeded the maximum power limit. Finally, the DE technique was compared to prototype-specific limits.

2.4.3 | Lookup-table for CNR-driven AEC

Three phantom thicknesses were used in creating the lookup table for the AEC model (18.6, 23.3, and 28.0 cm acrylic). CNR measurements were made using a reference object, which was a 1.5 mm thick, 6 mm diameter disk of MgCd alloy formulated to provide the same attenuation versus kV as a 350 mg I/mL iodinated contrast agent.[31,32] The signal difference created by the reference object approximates that of a 3 mm vessel filled with a 1:1 mixture of contrast agent and blood. This object was centered at the mid-thickness of the phantom within a 2 cm air gap. Measurements of iodine CNR in DE images were acquired using seven discrete tube voltage (kV) values (55, 60, 65, 75, 85, 105, 125 kV). Finer sampling was performed at the lower end of kV values as it was expected that the majority of AEC-selected tube techniques would utilize values in that range. For each kV value, six tube current–time product (mAs) values were used. The full range of investigated mAs values was 0.032–5.0 mAs; however, this range was adjusted in circumstances where detector electronic noise dominated the overall signal (low tube voltage, thicker phantoms), or if the detector became saturated (high tube voltage, thinner phantom). For all three phantom thicknesses, each unique combination of acquired kV and mAs values that passed tube technique constraints was used in forming the lookup table for the DE AEC model. Technical details for the prototype DE system are summarized in Table 1, including hardware specifications, real-time display capabilities, and the range of programmable x-ray tube parameters for the prototype fast kV-switching system.

The air kerma for each DE tube technique was based on tabulated air kerma measurements made at the interventional reference point (15 cm from the isocenter toward the x-ray tube). Air kerma was measured using eight discrete kV values (range: 55–125 kV) with fixed tube current (100 mA) and pulse width (10 ms) values. All measurements were acquired using a RadCal AccuGold meter with an AGMS-D+ sensor. To estimate the air kerma for any arbitrary tube technique (kV, mA, ms), air kerma measurements were interpolated across kV values using 2D smoothing splines. Air kerma was also assumed to scale linearly with mAs. The air kerma for a given DE tube technique was then reported as the total air kerma produced by a single DE image pair or the

TABLE 1 Summary of hardware (first column), real-time display capabilities (second column), and investigated range of x-ray tube parameters (third column) for the prototype fast kV-switching DE subtraction angiography system.

Prototype DE system hardware	Real-time display capabilities	Investigated range of x-ray tube parameters
Siemens Artis zee system	Dell 5810 XL tower, 72 GB RAM	Low tube voltage: 55–85 kV
Megalix Cat+ x-ray tube	GeForce 1080Ti GPU	High tube voltage: 105–125 kV
1.0 mm focal spot	Intel i217 network interface controller	Tube current: 10–500 mA
30 cm × 40 cm flat panel detector	Display live images (nominal 15 frame/s), or load from file	Low pulse width: 3.2–10 ms
0.308 mm element pitch (2 × 2 pixel binning)	Adjust DE material-canceling weighting factors, window/level	High pulse width: 3.2–10 ms

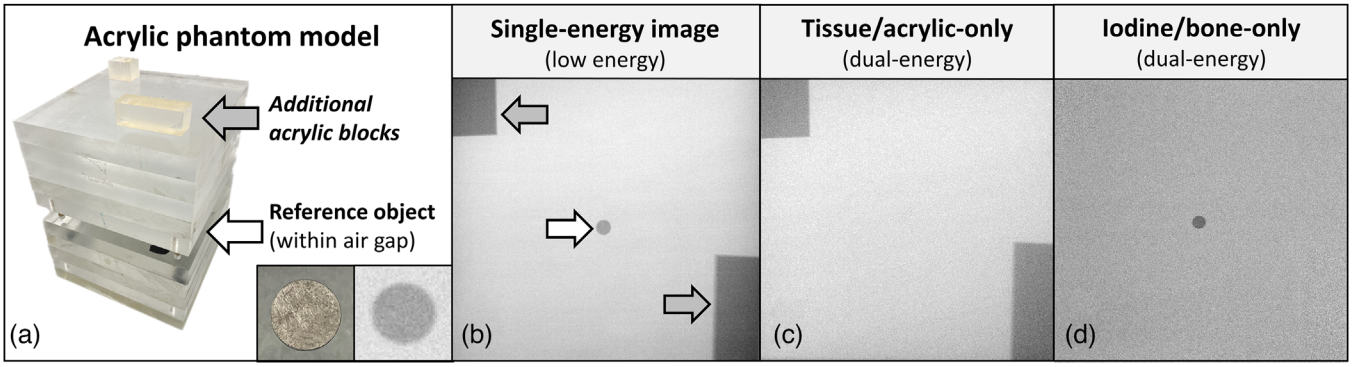

FIGURE 4 (a) Example phantom model used in creation of lookup table. The reference object is positioned in the center of the phantom within the air gap. Additional acrylic blocks placed on top of phantom facilitate determination of acrylic/tissue-canceling DE weighting factors. (b) Example low-energy image of phantom. Arrows point to the two regions used for material-cancellation, including the reference object used for measurements of iodine CNR. (c) Example tissue/acrylic only DE image. (d) Example iodine/bone-only DE image, which was used for measurements of iodine CNR.

sum of the air kerma from acquiring a single low- and high-energy projection image.

2.4.4 | DE image formation and iodine CNR measurements

Iodine/bone-only DE images processed with and without ACNR denoising were formed for every combination of the investigated imaging parameters. DE subtraction of background acrylic was accomplished with an empirically determined material-canceling weighting factor. In this scheme, the acrylic signal difference was minimized between an ROI containing background acrylic and ROIs containing background acrylic plus an additional 2.3-cm-thick acrylic block. Two such blocks were placed in opposite corners of the image. For every combination of investigated imaging parameters, acrylic-canceling weighting factors were computed for each corner of the image, and then the factors were averaged. Similarly, to form tissue/acrylic-only images, ROIs placed within and adjacent to the iodine reference object were used to empirically determine iodine-canceling weighting factors. Figure 4 shows an example phantom and single-energy image, as well as the corresponding tissue/acrylic-only and iodine/bone-only DE images.

All CNR measurements were computed as

$$CNR = \frac{|\mu_o - \mu_b|}{\sqrt{\sigma_o^2 + \sigma_b^2}}, \quad (5)$$

where μ_o, μ_b refer to the mean pixel values in ROIs placed within the iodine reference object and nearby background regions, respectively, and σ is the pixel standard deviation for the same ROIs. The mean CNR measurement ($n = 20$ frames) for every investigated set of imaging parameters was recorded for DE images processed with and without ACNR. The size of the averaging kernel used in ACNR denoising has previously been shown to correlate with the presence of high-spatial frequency artifacts in the final image.[10] Following this work, a kernel size of 7 × 7 pixels was used in this study. The ACNR factor p was determined by maximizing the CNR of the iodine reference object within the phantom.

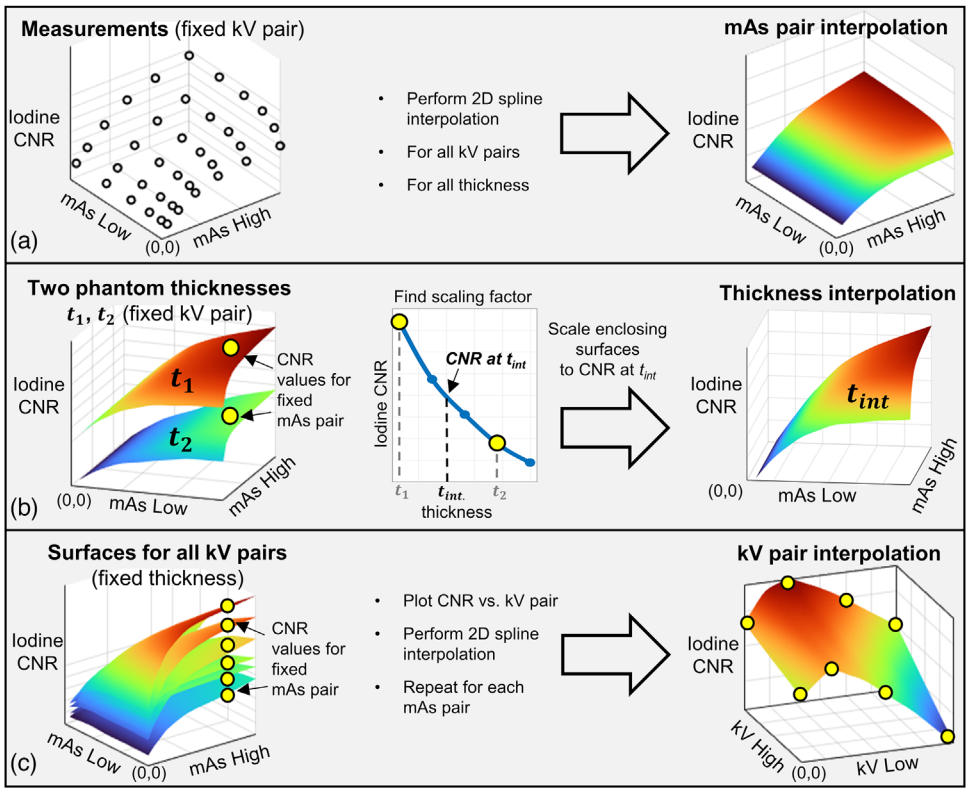

FIGURE 5 Interpolation schemes used in AEC models. For all graphs, an origin point (0, 0) was specified for reference. (a) Tube current product (mAs) pair interpolation uses a 2D spline interpolation versus CNR measurements to create a surface of CNR values. (b) Interpolation between acrylic thickness values was accomplished by scaling surfaces of CNR measurements (fixed kV pair) according to an empirical relationship describing CNR versus phantom thickness, which was separately measured for a single mAs pair. The scaled CNR surfaces were then averaged to generate a surface of CNR measurements at the interpolated thickness value. (c) Interpolation across kV pairs was achieved by plotting CNR measurements as a function of kV pair (kV low, kV high) for fixed combinations of mAs pair and phantom thickness. 2D spline interpolation was then performed to generate a surface of CNR measurements as a function of DE kV pair.

2.4.5 | Interpolation schemes for AEC look-up table

The measurements detailed in Section 2.4.4 provide reference-object iodine CNR in the DE image for a discrete number of DE tube techniques and phantom thicknesses. To estimate CNR for tube techniques and phantom thicknesses that were not directly measured, a multi-step interpolation process was applied. The initial step (Figure 5a) involves interpolating measured CNR values across the full mAs range for a fixed kV pair, in 0.01 mAs increments, using 2D smoothing splines. This process was performed for all the investigated DE kV pairs and phantom thicknesses. Next, these interpolated CNR values were scaled for different assumed acrylic thicknesses (Figure 5b). The scaling procedure was based upon the relationship between iodine CNR and phantom thickness, which was directly measured for all investigated kV values using a single mAs pair in a separate phantom experiment. Finally, kV pair interpolation (1 kV increments) was performed on iodine CNR measurements which have been scaled to the appropriate thickness value (Figure 5c). This was achieved by fixing the mAs pair and performing spline interpolations on iodine CNR measurements across all possible kV pair combinations. A schematic for this entire workflow is shown in Figure 5.

2.5 | Characterization of DE iodine CNR and dose efficiency

To validate the AEC model, the LUT was first used to generate a list of DE techniques, as well as predicted iodine CNR values. Next, three CNR requests (1.0, 2.0, 3.0) were specified for four acrylic thicknesses (21.0, 22.1, 25.6, and 26.8 cm). All the CNR requests and acrylic thickness values represented conditions that were not directly measured when forming the AEC LUT. To test that the AEC-selected techniques delivered CNRs that matched predictions, iodine CNR was directly measured ($n = 20$ frames) in acrylic phantoms containing the reference object (see Section 2.4). The percentage error between the predicted and measured CNR values was calculated for each CNR and thickness condition, and the mean and standard deviation of

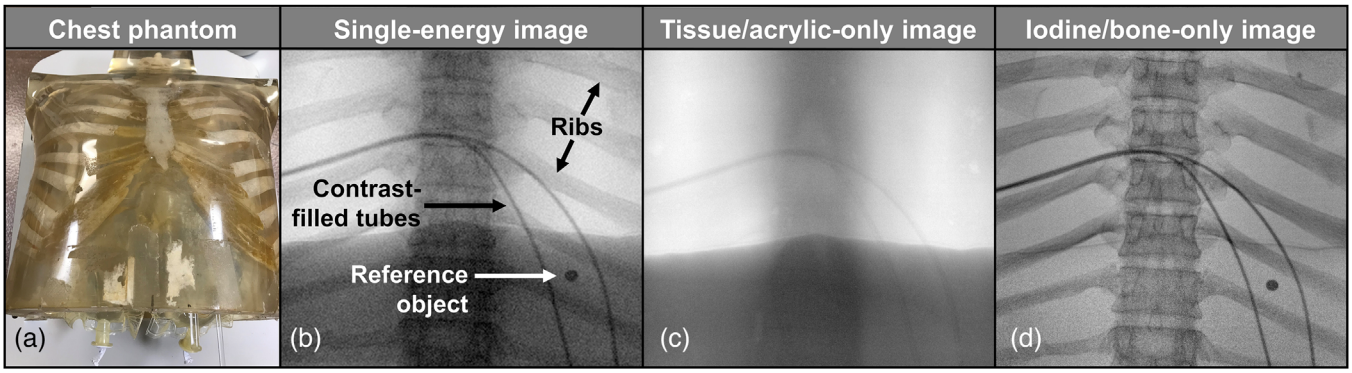

FIGURE 6 (a) Anthropomorphic chest phantom. (b) Low energy image, showing two 2 mm ID plastic tubes containing iodinated contrast agent and saline. (c) Tissue/acrylic-only DE image, which has been frame-averaged ($n = 16$). The image signal is associated with the greater acrylic thickness in the spine and abdominal regions as well as the plastic tube walls. (d) Iodine/bone-only image, which has been frame-averaged ($n = 16$). The image signal is due to iodine in the tubes, the iodine reference object, and bones.

these errors across all conditions was recorded. Dose efficiency was computed as the square of the measured iodine CNR divided by the dose,[33,34] where the dose was equal to the summed air kerma values for the high- and low-energy images used to form the DE image. Additionally, a dose allocation factor was reported for each AEC-generated technique. This factor was defined as the air kerma for the high-energy image divided by the total air kerma corresponding to the high- and low-energy image pair. Finally, DE techniques which yielded the maximum iodine CNR were generated for all acrylic thickness values.

This validation procedure was followed for the two separate AEC algorithms designed for DE imaging without and with ACNR denoising applied to the images. In the latter case, the tube techniques are referred to as DE+ACNR techniques. The ACNR-ML denoising method was applied to images generated with DE+ACNR techniques to assess potential increases in iodine CNR, and therefore dose efficiency, using ACNR-ML versus conventional ACNR denoising.

2.6 | Demonstration in anthropomorphic phantom

An anthropomorphic chest phantom containing ribs, acrylic, and a hollow chest cavity was imaged for demonstration purposes (Figure 6). Saline bags were placed within the hollow cavity to simulate a higher attenuating abdominal region. In the posterior–anterior projection, the acrylic-equivalent thickness as determined by x-ray transmission measurements was approximately 21.0 cm in the abdominal region, 16.2 cm in the lung region, and 20.5 cm in the spine region not overlapped by saline bags. Two 2 mm inner diameter (ID) iodine-filled acrylic tubes were placed within the phantom. Each tube was filled with a 1:1 by volume mixture of 350 mg I/mL Omnipaque and saline. The reference iodine-equivalent object, used in the AEC studies, was also placed in the phantom within the simulated abdominal region. DE images were acquired using two different tube techniques, corresponding to either a higher air kerma (63/125 kV, 200 mA, 9.9/3.2 ms; 0.45 mGy per DE image) or a lower air kerma acquisition (61/105 kV, 40 mA, 8/3.2 ms; 0.07 mGy per DE image). For both tube techniques, DE images were generated with and without application of both ACNR and ACNR-ML algorithms. Noise-reduction performance was evaluated by comparing the mean CNR value ($n = 20$ image frames) of the reference object.

3 | RESULTS

3.1 | Real-time display of DE images

The real-time workstation provided a display of DE images with a user-adjustable material cancellation factor. In stopwatch timing tests, the DE image display took an average of 9.5 ± 0.2 s to display all 124 DE image frames, corresponding to an achieved DE frame rate of 13.1 DE frames per second. When the same timing test was applied to the clinical system display, it was found that the clinical system displayed images at a rate of 12.9 frame pairs per second. Both frame rates were slightly below the nominal 15 frame/s rate because the prototype performs acquisition in a narrow-angle rotational mode involving slower gantry motion and lower frame rates at the beginning and end of the C-arm movement. (This rotation would not be present in a clinical implementation of 2D DE imaging.) The measured DE image frame rates were in close agreement with previous measurements using the RadCal detector, where the x-ray pulse rate was 26.3 pulse/s, or 13.2 pulse pairs per second.[19] The maximum processing and

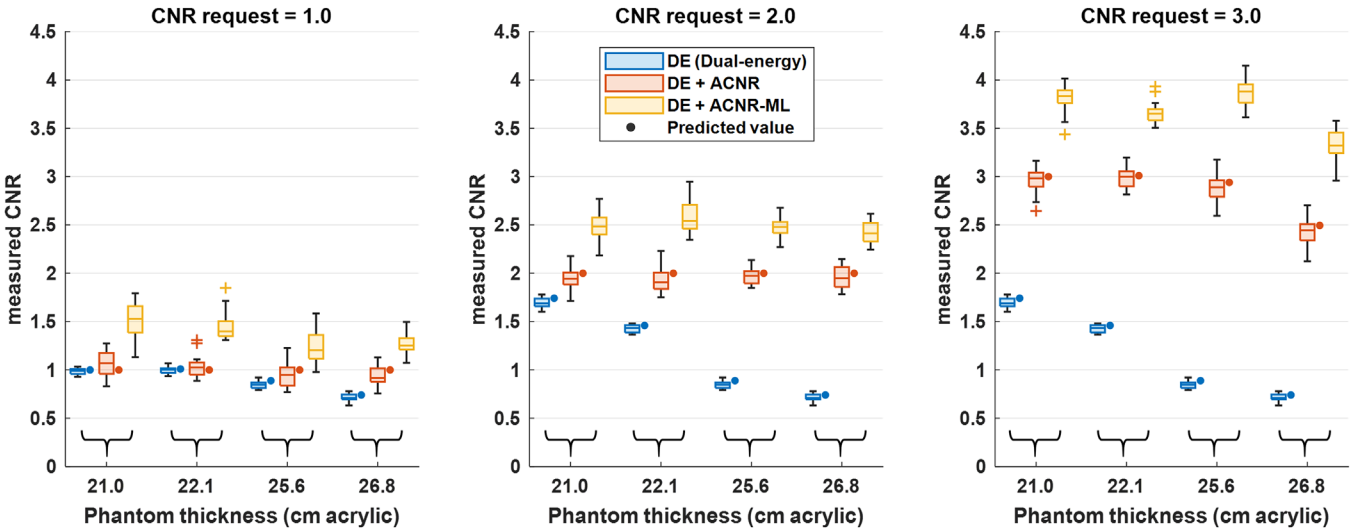

FIGURE 7 Validation of the AEC model, showing AEC-predicted CNR (closed circles) versus achieved CNR (boxplots) in phantom models. Each subplot represents a unique CNR request specified to the AEC. Each boxplot represents the interquartile range (IQR) of the direct measurements ($n = 20$). Median values are shown with solid horizontal lines, and outliers are represented using plus signs. CNR measured using AEC-generated DE techniques (blue boxplots) are compared with DE techniques generated using the ACNR algorithm (DE + ACNR; orange boxplots). The ACNR-ML algorithm (DE + ACNR-ML; yellow boxplots) was used to explore CNR increases relative to the ACNR algorithm. AEC-predicted CNR values differ from requested values if the CNR was unachievable due to tube output constraints.

display rate of the real-time workstation when reading images from local memory was 58.7 ± 0.03 DE frames per second. The measured percentage of raw frames dropped was 2.2% ± 0.5%.

3.2 | CNR-driven AEC model

AEC validation results are shown in Figure 7, for CNR requests of 1.0, 2.0, and 3.0. Each boxplot shows the spread of direct iodine CNR measurements ($n = 20$ image frames) for an imaging condition; the corresponding AEC-predicted value is shown alongside the boxplot as a closed circle. Note, the AEC algorithm is designed to select the DE technique which yields the requested CNR at the minimum air kerma, but if the requested CNR is unachievable due to x-ray tube constraints, then the algorithm instead selects the DE technique which yields the maximum CNR. Therefore, the predicted CNR in this validation study was either the requested CNR, or the maximum predicted CNR. Also note that since ACNR-ML denoising was only used to study potential increases in CNR when using an ACNR technique, the ACNR-ML boxplots do not have corresponding CNR predictions. For all investigated phantom thicknesses and CNR requests, the AEC-predicted CNR values were within 3.5% ± 1.6% (mean ± standard deviation) of measured values for standard DE tube techniques and 2.1% ± 3.3% for DE + ACNR techniques. Without ACNR denoising applied, the AEC-predicted CNR matched the CNR request for the two of the investigated cases (CNR request of 1.0, acrylic thickness of 21.0 and 22.1 cm), but for other cases the predicted CNR was below the requested CNR due to tube output constraints. In contrast, when ACNR denoising was applied, AEC-generated DE techniques were able to deliver the requested CNR in all but two cases (CNR request of 3.0, ≥25.6 cm acrylic thickness). Furthermore, when the ACNR-ML algorithm was applied, every CNR request across all acrylic thickness values was achieved. The application of ACNR-ML increased iodine CNR by 1.23 – 1.42x (mean increase: 1.32x) compared to processing with standard ACNR.

3.3 | AEC-selected x-ray tube techniques

Fast kV-switching DE tube techniques were generated using the developed AEC model by iteratively varying the CNR request and patient thickness model inputs. For brevity, the techniques corresponding to the 21.0 and 26.8 cm acrylic phantom sizes are shown in Table 2 for all three CNR requests (CNR of 1.0, 2.0, 3.0). These techniques correspond to a portion of the DE tube techniques which were validated in separate phantom studies in Section 3.2.

Within the selected measurement conditions, DE and DE + ACNR tube techniques showed similarities in the chosen tube voltage pair values, which were typically around 62–65 kV for the low energy and 125 kV for the high energy. The reported kV pairs are generally consistent with results published in recent work, where low tube voltages are expected to be between 60 and 70 kV and high voltages at or above 120 kV.[18] The pulse widths were commonly 10 ms at low energy and 3.2 ms

TABLE 2 Selected DE tube techniques taken from the AEC validation study.

Technique	Phantom thickness (cm acrylic)	CNR request (reference object)	Tube voltage pair (kV low, kV high)	Tube current (mA)	Pulse width pair (ms low, ms high)	Kerma (mGy per DE image)	Dose allocation factor (high/total)
Standard dual-energy **(DE)**	21.0	1.0	63/125	200	9.9/3.2	0.45	0.57
		2.0, 3.0[a]	62/125	490	10/5.0	1.44	0.68
	26.8	1.0, 2.0, 3.0[a]	65/125	480	10/5.8	1.62	0.69
Denoised dual-energy **(DE+ACNR)**	21.0	1.0	63/107	40	8.0/3.2	0.07	0.55
		2.0	55/122	110	10/3.2	0.21	0.64
		3.0	64/125	200	10/3.2	0.46	0.55
	26.8	1.0	64/125	130	9.5/3.2	0.29	0.57
		2.0	64/125	440	9.7/3.2	1.00	0.56
		3.0[a]	65/125	440	10/9.6	2.15	0.78

Note: Both standard DE and denoised DE (DE + ACNR) techniques are reported for the thinner (21.0 cm) and thicker (26.8 cm) acrylic phantom sizes, for all three CNR requests. Tube technique information is displayed in terms of the low/high energy voltage pair, tube current value, and low/high pulse width pair. Air kerma is reported per image pair used to form a DE image, at the interventional reference point.

[a]The requested iodine CNR was not achieved; in these scenarios, the AEC selects the DE tube technique which yields the highest iodine CNR value for the given acrylic thickness, while adhering to tube technique constraints.

at high energy. These pulse widths represent the upper and lower limits of the DE prototype, respectively, and indicate that the algorithm tends to allocate higher mAs values to the low energy acquisitions. The mA value varied depending on the phantom thickness, CNR request, and whether or not ACNR denoising was applied. In the DE+ACNR case, a greater range of reference object iodine CNRs was achieved, and CNR requests were satisfied with a lower tube current and lower air kerma per DE image compared to the non-denoised, standard DE case (e.g., for 21.0 cm acrylic and CNR = 1.0, the ACNR approach required 40 mA, 0.07 mGy versus 200 mA, 0.45 mGy). Techniques shown for DE + ACNR delivered the requested CNR, apart from the CNR request of 3.0 for the 26.8 cm phantom.

3.4 | Dose efficiency and maximum iodine CNR

DE tube techniques were also evaluated in terms of their dose efficiency and maximum reference object CNR values (i.e., maximum achieved within tube constraints). Figure 8 shows plots of both metrics, comparing standard AEC-generated DE techniques with DE techniques that have been processed with ACNR (DE + ACNR) and the ACNR-ML algorithm (DE + ACNR-ML). All calculated dose efficiencies were grouped across CNR requests for each acrylic thickness value ($n = 60$ measurements per boxplot), whereas maximum iodine CNR values ($n = 20$ measurements per boxplot) are shown versus acrylic thickness.

When the dose efficiency of DE + ACNR was compared to standard DE for individual imaging scenarios, the ratio of dose efficiencies was 9.37 ± 2.08 (mean ± standard deviation). When the dose efficiency of DE + ACNR-ML was compared to standard DE, the ratio was 16.11 ± 2.99. When the ratio of maximum CNR values for each imaging scenario was compared, DE + ACNR increased iodine CNR by 3.29 ± 0.21 (mean ± standard deviation) compared to standard DE. Using ACNR-ML, the iodine CNR was increased by 4.46 ± 0.31 relative to standard DE.

3.5 | Phantom demonstration study

Figure 9 shows example iodine/bone-only chest phantom images for standard DE, DE with ACNR denoising, and DE with ACNR-ML. Equivalent windowing is applied to all cases. For both the higher and lower air kerma levels, the image noise was highest in the standard non-denoised DE case. With the application of either noise-reduction approach, image noise was reduced. CNR measurements of the reference object showed that DE images processed with ACNR-ML achieved the highest iodine CNR values in both high and low air kerma scans (4.97 ± 0.21 and 1.84 ± 0.16, respectively) compared to conventional ACNR (4.12 ± 0.19 and 1.45 ± 0.24) and standard DE (1.24 ± 0.07 and 0.31 ± 0.05). The measured CNR improvement using ACNR-ML over the conventional ACNR approach is consistent with previously published comparisons of DE noise reduction performance in a separate phantom study.[20]

4 | DISCUSSION

This study reports on the development of a prototype fast kV-switching DE subtraction angiography system. The intended purpose of the prototype system is to

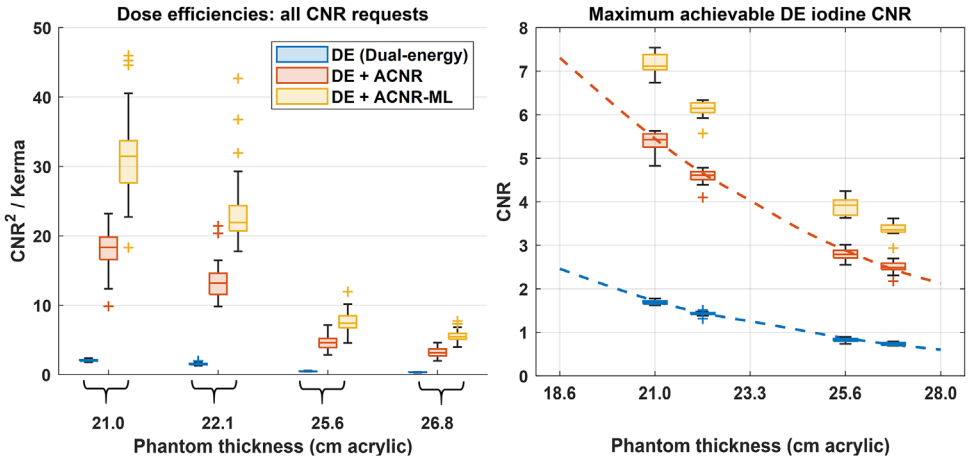

FIGURE 8 (Left) Dose efficiencies of DE tube techniques generated during the AEC validation study. Each boxplot contains dose efficiencies calculated across all three CNR requests ($n = 60$). (Right) Maximum achieved CNR, as a function of phantom thickness. Boxplots show the spread of direct measurements ($n = 20$). Dashed lines indicate smoothing splines of AEC predictions.

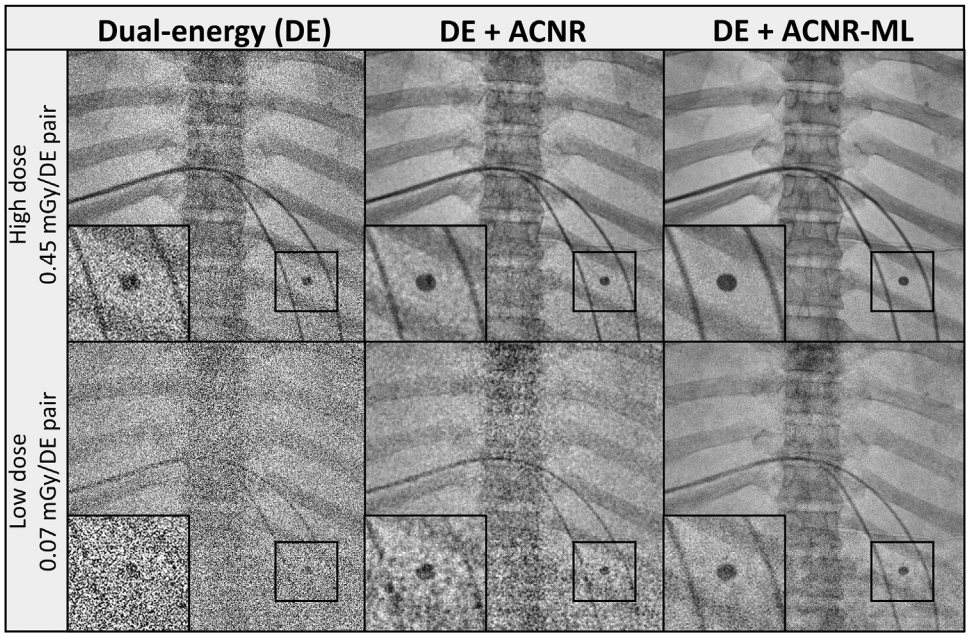

FIGURE 9 Iodine/bone-only DE images taken of the chest phantom. Columns show processing technique; rows correspond to higher dose (top row), and lower dose (bottom row) acquisitions, where dose is reported as air kerma at the interventional reference point. ROIs show the reference object, ribs, and contrast-filled tubes in an abdominal region with a 21.0 cm acrylic-equivalent thickness.

investigate real-time DE imaging during image-guided interventions. In contrast to alternative approaches to DE imaging in the interventional suite, such as dual-layer detectors and photon counting detectors, this prototype uses a standard, clinically available interventional C-arm equipped with special x-ray tube control software. Beyond its availability, fast kV-switching may offer additional benefits such as improved iodine signal-difference-to-noise ratio relative to multi-layer detectors.[18] This work presents necessary technical developments including a means for real-time display, a strategy for noise-reduction, and a CNR-driven automatic exposure control to guide DE technique selection.

For this study, the ACNR algorithm was used as the basis for image noise reduction. This algorithm is well-suited for real-time angiographic procedures and does not present the risk of altering the vascular signal since the denoising operation occurs on the tissue-only image. A variant of this approach, ACNR-ML, utilizes machine-learning instead of a low-pass filter in the denoising operation. Results from the characterization

of the CNR-driven AEC model show large reductions in air kerma using either denoising approach, resulting in large increases in DE dose efficiencies. In this work, we have also shown that ACNR-ML is capable of boosting iodine CNR values relative to the conventional ACNR approach. Previous work characterizing both denoising approaches showed that the ACNR-ML approach maintains a noise texture more consistent with the original projection images when compared to ACNR.[20]

Several aspects of the prototype DE system warrant further investigation. The reported AEC framework can be expanded with additional measurements to include acrylic thickness values above 28.0 cm, which may be needed to account for larger patient sizes. Additionally, the AEC framework can also be expanded upon to include factors such as blurring, imaging different materials of interest, or changing object size, which has recently been the focus of AEC models for single-energy imaging techniques.[35,36] While the expansion of the current AEC framework could utilize the experimental methods reported in this work, the use of simulation-based studies may be needed to supplement experiments as the number of free parameters in the AEC model increases. When using the developed AEC model in practice, the method outlined in Section 2.4.1 could be used to estimate the thickness of the patient in terms of an acrylic-equivalent thickness. However, this approach does not account for differences in the scatter conditions, which may affect CNR prediction accuracy. Modeling of scatter for a heterogenous patient is a potential way to address this issue. Additionally, the AEC model could be adapted to include the performance of newer interventional platforms and x-ray tubes, which may have different tube technique constraints and therefore may enable higher DE iodine CNR values.

In this study, a large increase in DE dose efficiency was observed when using either the ACNR or ACNR-ML noise-reduction approach. However, this study does not compare the dose efficiency of DE techniques with that of DSA imaging. Previous work has demonstrated that parity in dose efficiency is achievable, although this can be challenging to achieve under realistic scatter conditions, and detector electronic noise must be low.[37] Post-processing via the ACNR denoising algorithm is one means of improving iodine CNR. Another approach which may be used in conjunction with denoising algorithms is the selective filtration of the high-energy x-ray spectrum.[38] To investigate this claim, a uniform acrylic phantom (23.3 cm thickness) containing the iodine-equivalent reference object (350 mg I/mL density) was sequentially imaged using two different techniques (65 kV, 600 mA, 10 ms; and 125 kV, 430 mA, 10 ms) on the Siemens Artis zee platform. In the high-energy acquisition, 0.9 mm of copper filtration was applied to the x-ray spectrum. For this scenario, it was found that the DE dose efficiency was increased by 3.9 times the original value with the addition of the copper filtration. While the current fast kV-switching prototype does not have a means to selectively filter the high energy projections, the use of a rapidly rotating or translating filter system attached to the C-arm gantry may enable this feature. In addition to selective filtration, a fully realized clinical implementation of this prototype DE system should integrate noise reduction strategies and the AEC model into the real-time workstation for a seamless user experience.

5 | CONCLUSION

A prototype DE subtraction angiography system using fast kV-switching was implemented on a clinically available interventional C-arm platform without modification of system hardware. The prototype system has capabilities to display DE images in real-time, and the investigated noise-reduction strategies show promise to reduce image noise without compromising vascular signal during 2D angiographic procedures. A CNR-driven AEC algorithm was developed to characterize the performance of both noise-reduction algorithms, and guide future studies utilizing DE subtraction schemes. The in-house denoising method, ACNR-ML, enabled further increases in iodine CNR. Future experiments should be performed to assess the performance of the investigated DE platform in vivo.

ACKNOWLEDGMENTS

Research reported in this publication was supported by a sponsored research agreement with Siemens Healthineers, the National Institutes of Health grant number R21 EB023008, and the National Cancer Institute of the National Institutes of Health under award number T32CA009206. The content in this paper is solely the responsibility of the authors and does not represent the official views of the National Institutes of Health or Siemens Healthineers. The concepts presented in this paper are based on research and are not commercially available.

CONFLICT OF INTEREST STATEMENT

Authors Michael Speidel and Paul Laeseke have sponsored research agreements with Siemens Healthineers. James Scheuermann is a full-time employee of Siemens Healthineers.

DATA AVAILABILITY STATEMENT

The data that support the findings of this study are available from the corresponding author upon reasonable request.

REFERENCES

1. Macovski A, Alvarez RE, Chan JLH, Stonestrom JP, Zatz LM. Energy dependent reconstruction in X-ray computerized tomography. *Comput Biol Med*. 1976;6(4):325-336. doi:10.1016/0010-4825(76)90069-X
2. Fischbach F, Freund T, Röttgen R, Engert U, Felix R, Ricke J. Dual-energy chest radiography with a flat-panel digital detector: revealing calcified chest abnormalities. *Am J Roentgenol*. 2003;181(6):1519-1524.
3. Gilkeson RC, Sachs PB. Dual energy subtraction digital radiography: technical considerations, clinical applications, and imaging pitfalls. *J Thorac Imaging*. 2006;21(4):303-313. doi:10.1097/01.rti.0000213646.34417.be
4. Lewiecki EM, Binkley N, Morgan SL, et al. Best practices for dual-energy x-ray absorptiometry measurement and reporting: international society for clinical densitometry guidance. *J Clin Densitom*. 2016;19(2):127-140. doi:10.1016/j.jocd.2016.03.003
5. McCollough CH, Leng S, Yu L, Fletcher JG. Dual-and multi-energy ct: principles, technical approaches, and clinical applications. *Radiology*. 2015;276(3):637-53. doi:10.1148/radiol.2015142631
6. Goo HW, Goo JM. Dual-energy CT: new horizon in medical imaging. *Korean J Radiol*. 2017;18(4):555. doi:10.3348/kjr.2017.18.4.555
7. Hamid S, Nasir MU, So A, Andrews G, Nicolaou S, Qamar SR. Clinical applications of dual-energy CT. *Korean J Radiol*. 2021;22(6):970. doi:10.3348/kjr.2020.0996
8. Müller K, Datta S, Ahmad M, et al. Interventional dual-energy imaging-Feasibility of rapid kV-switching on a C-arm CT system. *Med Phys*. 2016;43(10):5537. doi:10.1118/1.4962929
9. Van Lysel MS, Miller WP, Senior DG, Gupta VK, Ende DJ, Albright DJ. Left ventricular dual-energy digital subtraction angiography: a motion immune digital subtraction technique. *Int J Card Imaging*. 1991;7(1):55-65.
10. McCollough CH, Van Lysel MS, Peppler WW, Mistretta CA. A correlated noise reduction algorithm for dual-energy digital subtraction angiography. *Med Phys*. 1989;16(6):873-880.
11. Shi L, Lu M, Bennett NR, et al. Characterization and potential applications of a dual-layer flat-panel detector. *Med Phys*. 2020;47(8):3332-3343. doi:10.1002/mp.14211
12. Cai EY, De Caro C, Treb K, Li K. Benefits of using removable filters in dual-layer flat panel detectors. *Phys Med Biol*. 2023;68(8):085013. doi:10.1088/1361-6560/acc77d
13. Han JC, Kim HK, Kim DW, et al. Single-shot dual-energy x-ray imaging with a flat-panel sandwich detector for preclinical imaging. *Curr Appl Phys*. 2014;14(12):1734-1742. doi:10.1016/j.cap.2014.10.012
14. Treb K, Ji X, Feng M, et al. A C-arm photon counting CT prototype with volumetric coverage using multi-sweep step-and-shoot acquisitions. *Phys Med Biol*. 2022;67(21):215003. doi:10.1088/1361-6560/ac950d
15. Treb K, Hämisch Y, Ullberg C, Zhang R, Li K. Photon counting-energy integrating hybrid flat panel detector systems for image-guided interventions: an experimental proof-of-concept. *Phys Med Biol*. 2023;68(13):135009. doi:10.1088/1361-6560/acddc7
16. Ahmad M, Fahrig R, Pung L, et al. Assessment of a photon-counting detector for a dual-energy C-arm angiographic system. *Med Phys*. 2017;44(11):5938-5948. doi:10.1002/mp.12517
17. Williams KA, Shields A, Setlur Nagesh SV, et al. Angiographic velocimetry analysis using contrast dilution gradient method with a 1000 frames per second photon-counting detector. *J Med Imaging*. 2023;10(03):033502. doi:10.1117/1.JMI.10.3.033502
18. Aubert S, Tanguay J. Experimental optimization of single-exposure dual-energy angiography with photon-counting x-ray detectors. *Med Phys*. 2023;50(2):763-777. doi:10.1002/mp.16079
19. Speidel MA, Burton CS, Nikolau EP, Schafer S, Laeseke PF. Prototype system for interventional dual-energy subtraction angiography. Proc SPIE Int Soc Opt Eng; 2019:10951:109511U. doi:10.1117/12.2512956
20. Nikolau EP, Whitehead JF, Wagner MG, Laeseke PF, Speidel MA. Dual-energy image noise reduction on an interventional x-ray system. In: Zhao W, Yu L, eds. *Medical Imaging 2022: Physics of Medical Imaging*. SPIE; 2022:22. doi:10.1117/12.2612259
21. Brody WR, Butt G, Hall A, Macovski A. A method for selective tissue and bone visualization using dual energy scanned projection radiography. *Med Phys*. 1981;8(3):353-357. doi:10.1118/1.594957
22. Romadanov I, Sattarivand M. Adaptive noise reduction for dual-energy x-ray imaging based on spatial variations in beam attenuation. *Phys Med Biol*. 2020;65(24):245023. doi:10.1088/1361-6560/ab9e57
23. Ducote JL, Xu T, Molloi S. Optimization of a flat-panel based real time dual-energy system for cardiac imaging: real time flat-panel dual-energy. *Med Phys*. 2006;33(6 Part1):1562-1568. doi:10.1118/1.2174131
24. Jain A, Bansal R, Kumar A, Singh K. A comparative study of visual and auditory reaction times on the basis of gender and physical activity levels of medical first year students. *Int J Appl Basic Med Res*. 2015;5(2):124. doi:10.4103/2229-516X.157168
25. Kalender WA, Klotz E, Kostaridou L. An algorithm for noise suppression in dual energy CT material density images. *IEEE Trans Med Imaging*. 1988;7(3):218-224. doi:10.1109/42.7785
26. Warp RJ, Dobbins JT. Quantitative evaluation of noise reduction strategies in dual-energy imaging. *Med Phys*. 2003;30(2):190-198. doi:10.1118/1.1538232
27. Richard S, Siewerdsen JH. Cascaded systems analysis of noise reduction algorithms in dual-energy imaging. *Med Phys*. 2008;35(2):586-601. doi:10.1118/1.2826556
28. Kaur M, Wagstaff P, Mostafavi H, et al. Effect of different noise reduction techniques and template matching parameters on markerless tumor tracking using dual-energy imaging. *J Appl Clin Med Phys*. 2022;23(12):e13821. doi:10.1002/acm2.13821
29. Ronneberger O, Fischer P, Brox T. U-Net: convolutional Networks for Biomedical Image Segmentation; 2015. doi:10.48550/ARXIV.1505.04597
30. Whitehead JF, Nikolau EP, Periyasamy S, et al. Simulation of hepatic arteries and synthesis of 2D fluoroscopic images for interventional imaging studies. In: *Proc SPIE Vol. 11312, Medical Imaging 2020: Physics of Medical Imaging*; 2020:11312W. doi:10.1117/12.2549570
31. Betts T, Speidel M, Van Lysel M. Metallic phantom material is radiographically equivalent to iodine contrast media. Paper presented at: Radiological Society of North America 2005 Scientific Assembly and Annual Meeting, November 27 - December 2, 2005, Chicago, IL. Accessed September 10, 2024 http://archive.rsna.org/2005/4412969.html
32. Betts TD. *Metallic Alloys for Use in Radiographic Phantoms*. University of Wisconsin-Madison; 2010.
33. Tapiovaara MJ. Review of relationships between physical measurements and user evaluation of image quality. *Radiat Prot Dosimetry*. 2008;129(1-3):244-248. doi:10.1093/rpd/ncn009
34. Gislason AJ, Davies AG, Cowen AR. Dose optimization in pediatric cardiac x-ray imaging: dose optimization in pediatric cardiac x-ray imaging. *Med Phys*. 2010;37(10):5258-5269. doi:10.1118/1.3488911
35. Werncke T, Kemling M, Tashenov S, et al. Comparison of a contrast-to-noise ratio-driven exposure control and a regular detector dose-driven exposure control in abdominal imaging in a clinical angiography system. *Med Phys*. 2021;48(12):7641-7656. doi:10.1002/mp.15288
36. Werncke T, Kemling M, Tashenov S, et al. Impact of a contrast-to-noise ratio driven and material specific exposure control on

image quality and radiation exposure in angiography. *Phys Med Biol*. 2021;66(6):065020. doi:10.1088/1361-6560/abe83a
37. Burton CS, Mayo JR, Cunningham IA. Energy subtraction angiography is comparable to digital subtraction angiography in terms of iodine rose SNR. *Med Phys*. 2016;43(11):5925-5933. doi:10.1118/1.4962651
38. Krauss B, Grant KL, Schmidt BT, Flohr TG. The importance of spectral separation: an assessment of dual-energy spectral separation for quantitative ability and dose efficiency. *Invest Radiol*. 2015;50(2):114-118. doi:10.1097/RLI.0000000000000109

How to cite this article: Nikolau EP, Whitehead JF, Wagner MG, Scheuermann JR, Laeseke PF, Speidel MA. Technique selection and technical developments for 2D dual-energy subtraction angiography on an interventional C-arm. *Med Phys*. 2025;52:3228–3242. https://doi.org/10.1002/mp.17661